Ultramicroscopy 000 (2017) 1–8

Contents lists available at ScienceDirect

Ultramicroscopy

journal homepage: www.elsevier.com/locate/ultramic

Simulation in elemental mapping using aberration-corrected electron microscopy

L.J. Allen

School of Physics, University of Melbourne, Parkville, Victoria 3010, Australia

ARTICLE INFO

Article history:
Received 30 August 2016
Revised 24 February 2017
Accepted 1 March 2017
Available online xxx

Keywords:
Atomic resolution imaging
Electron energy-loss spectroscopy
Energy-dispersive X-ray analysis
Energy-filtered transmission electron microscopy
Elemental mapping

ABSTRACT

Elemental mapping at the atomic scale in aberration-corrected electron microscopes is becoming increasingly widely used. In this paper we describe the essential role of simulation in understanding the underlying physics and thus in correctly interpreting these maps, both qualitatively and quantitatively.

1. Introduction

The use of electron energy-loss spectroscopy (EELS) to determine the valence of an atom occupying a particular crystal lattice site was demonstrated by Taftø and Krivanek in the early 1980s [1]. Pioneering developments in instrumentation for EELS and energy-loss imaging and the design and implementation of a post-column imaging filter are described in papers by Ondrej Krivanek and coworkers in the early 1990s [2,3], with the stated aim of fast imaging and elemental mapping in scanning transmission electron microscopy (STEM) mode. This led to a number of milestones and ideas relating to EELS and elemental mapping in which Ondrej Krivanek played a pivotal role. These include an exploration of spatial resolution in energy-filtered transmission electron microscopy (EFTEM) elemental maps [4]; the spectroscopic imaging of a single atom within a bulk solid using STEM [5]; an exploration of annular dark-field (ADF) imaging and EELS at low primary energies [6]; and atom-by-atom structural and chemical (elemental) analysis using ADF imaging [7].

This pioneering work, together with the development of aberration-corrected electron microscopy, another area to which Ondrej Krivanek has made major contributions, has led to elemental mapping at the atomic scale becoming a widely used technique. Elemental mapping in two dimensions at atomic resolution in STEM, using EELS based on inner-shell ionization, was first demonstrated in 2007 [8,9] and rapidly evolved as a useful tool – see for example [10–14] where, in particular, Ref. [13] is a comprehensive review of atomic-resolution core-level spectroscopy in STEM. The rest of this review will focus on elemental mapping in two dimensions and, in particular on understanding the physics behind such maps via simulation. For more general discussion of STEM EELS the reader is referred to Refs. [15,16].

Unless the detector collection angle is very large, EELS is a partially-coherent imaging mode – by which we mean that it depends not only on the probe intensity distribution but also on its phase – and this may hinder a simple direct interpretation of the elemental maps. In STEM EELS we integrate up over a suitable energy-loss window to form an elemental map. In Fig. 1(a) we show a Z-contrast image of $Bi_{0.5}Sr_{0.5}MnO_3$ oriented along the ⟨001⟩ direction, extracted from one of the seminal STEM EELS papers [8]. Columns containing Bi and Sr atoms are clearly evident, as are columns containing both Mn and O atoms. Since the Z-contrast signal scales roughly as Z^2, the pure O columns are not evident in the image. However, the O columns can be seen by integrating the signal obtained for the O K-edge in an EELS spectrometer over an energy window of 30 eV above the ionization threshold, as can be seen in Fig. 1(b), also extracted from Ref. [8]. The data in Fig. 1 were acquired using the VG HB501 scanning transmission electron microscope at the SuperSTEM facility in the UK, a system fitted with a Nion spherical aberration corrector.

As an alternative to STEM EELS one can use energy-dispersive X-ray (EDX) analysis, detecting the X-rays which are emitted subsequent to ionization as the STEM probe is scanned across the specimen. Since EDX elemental mapping is an incoherent mode

E-mail address: lja@unimelb.edu.au

http://dx.doi.org/10.1016/j.ultramic.2017.03.001
0304-3991/

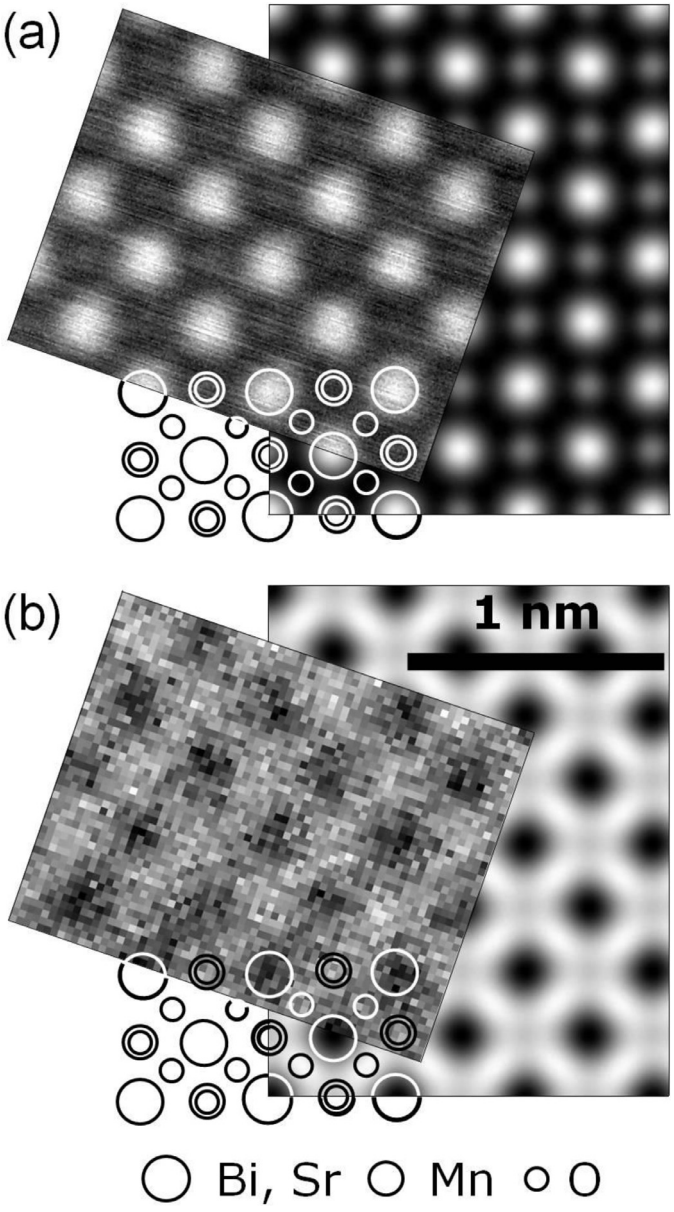

Fig. 1. Comparison between experiments (the tilted images) and simulations of $Bi_{0.5}Sr_{0.5}MnO_3$ oriented along the [001] zone axis. (a) Z-contrast, (b) the O K-edge EELS elemental map. The atomic structure is indicated. The EELS elemental map was generated by integrating the EELS spectra over a 30 eV window above the ionization threshold. The simulations assume a 330 Å thick sample. Experimental details are given in Ref. [8].

of imaging, image interpretation may be expected to be simpler than for EELS. In STEM EDX we are detecting X-rays generated when holes are filled post ionization and all possible kinematics associated with ionization are sampled, since there is no detector aperture as in EELS to exclude electrons inelastically scattered to larger angles. Therefore, the cross section for EDX is proportional to that for an EELS detector spanning the whole solid angle and integrated up over all possible energy losses. Furthermore, the larger effective energy window in EDX, relative to the smaller window usual in EELS, leads to an increased localization of the signal in an EDX elemental map. Thus EDX imaging is more reminiscent of the widely used technique of ADF or Z-contrast imaging, but with the advantage that elemental information is directly available for a range of different elements and X-ray peaks. A further advantage of EDX mapping relative to EELS is the accessibility of higher energy-loss peaks and their associated increased localization. The first two-dimensional atomic resolution elemental maps based on EDX were published as recently as 2010 [17,18] and considerable improvements in the quality of such data followed rapidly [19], although signal-to-noise ratios are generally lower than for EELS. Quantification in STEM EDX has recently been addressed [20–23].

Elemental maps displaying features at atomic scale can also be obtained in conventional transmission electron microscopy (CTEM) in EFTEM mode, see for example Ref. [24], and in later work the advent of chromatic aberration correction facilitates this greatly [25,26]. However, quantum mechanical calculations from first principles need to be done in tandem with the experiments to understand the physical information encoded in the images; in particular this need is due to the preservation of elastic contrast. Ways of ameliorating the preservation of elastic contrast have recently been proposed [27].

Understanding the effects of the channelling and thermal diffuse scattering of the probing electrons on elemental maps is key to their correct interpretation, particularly for crystalline specimens. For example, it may be tempting to assume that a STEM probe, when positioned above a particular column of atoms in a specimen, interacts only with that column and, furthermore, in a uniform way with all atoms in the column. This is only reasonable in the limit of a thin specimen, with the probe focused on or near the entrance surface. It is not generally appreciated that, for elemental maps based on less tightly bound atomic orbitals, the ionization interaction can be quite delocalized and that ionization may occur even when the probe intensity on a particular atom is small [28,29]. In loose terms, the atom reaches out to the probe. Furthermore, thermal diffuse scattering can lead the unwary to interpret an elemental map as either suggesting too few [8] or too many [30] atoms of a particular species in an atomic column. Atomic scale elemental maps are not necessarily atomic resolution maps in the sense that they directly and quantitatively map where the atoms are and what they are. Therefore, simulations are an essential part of confidently making correct interpretations of elemental maps. In the next section we will discuss the theoretical framework for such simulations.

2. Inner-shell ionization in the quantum excitation of phonons model

A general scheme to calculate elemental maps is provided by working within the context of the quantum excitation of phonons (QEP) model [31,32]. An important feature of the QEP model is that signals based on ionization arising from both elastically and thermally scattered electrons can be calculated separately and this can yield important physical insights.

The fraction of the incident electrons that are involved in ionization events associated with a particular edge may be expressed in the form [31,33]:

$$F(\mathbf{P}) = \frac{2\pi}{h\nu} \sum_{j,i} \iint \psi^*_{0,j}(\mathbf{P}, \mathbf{r}, z_i) W_j(\mathbf{r}, \mathbf{r}', z_i) \psi_{0,j}(\mathbf{P}, \mathbf{r}', z_i) d\mathbf{r} d\mathbf{r}'. \quad (1)$$

The functional dependence denoted by **P** in Eq. (1) represents the probe position **R** on the surface of the specimen in STEM and in CTEM it could represent the tilt of the incident beam specified by the tangential component of the wave vector of the incident electrons $\mathbf{k}_{0t}$. The speed $v = hk_0/m$, with k_0 the wave number of the incoming electron and m its mass. The summation over i is over slices in the specimen and that over j refers to different possible atomic configurations "seen" by the incident electron in the QEP model. The "auxilliary functions" $\psi_{0,j}(\mathbf{P}, \mathbf{r}, z_i)$ associated with the probing electron, and where the co-ordinate **r** refers to a plane perpendicular to the optical axis, are calculated for the particular atomic configuration labelled by j. The nonlocal potentials in

Please cite this article as: L.J. Allen, Simulation in elemental mapping using aberration-corrected electron microscopy, Ultramicroscopy (2017), http://dx.doi.org/10.1016/j.ultramic.2017.03.001

Eq. (1) are given by

$$W(\mathbf{r},\mathbf{r}',z_i)=\frac{2\pi m}{h^2}\sum_{n\neq 0}\frac{1}{k_n}H^*_{n0}(\mathbf{r},z_i)H_{n0}(\mathbf{r}',z_i)\int_D e^{2\pi i\mathbf{q}\cdot(\mathbf{r}-\mathbf{r}')}d\mathbf{q}\ , \quad (2)$$

where we have dropped the subscript j. This is done since the transition potentials $H^*_{n0}(\mathbf{r},z_i)$ for ionization extend over a substantially larger range than the scale of atomic thermal motion and it is a good approximation to use transition potentials at the equilibrium positions of the atoms and modify only the $\psi_{0,j}(\mathbf{R},\mathbf{r},z_i)$ in Eq. (1) for the different configurations. The transition potentials $H_{n0}(\mathbf{r},z_i)$ in Eq. (2) for a transition of the specimen (atom being ionized) from an initial state labelled 0 to a final state labelled by n (corresponding to an unbound electron), are given in three dimensions by

$$H_{n0}(\mathbf{x})=\frac{e^2}{4\pi\epsilon_0}\int u^*_n(\mathbf{x}')\frac{1}{|\mathbf{x}-\mathbf{x}'|}u_0(\mathbf{x}')d\mathbf{x}'\ , \quad (3)$$

where $u_n(\mathbf{x})$ and $u_0(\mathbf{x})$ are the initial and final state wave functions and $\mathbf{x}$ is a vector in three dimensions. The summation over n is over all pertinent final states. In Eq. (2) k_n is the wave number of the inelastically scattered electrons after such a transition. The prefactor in Eq. (3) contains the magnitude of the charge on an electron e and the permittivity of free space ϵ_0. It is assumed that the inelastic transition effectively occurs in vacuum but this can be generalized, if needed, by incorporating a suitable dielectric function in Eq. (3). The projected transition potentials $H_{n0}(\mathbf{r},z_i)$ in Eq. (2) are then obtained as follows [34–36]:

$$H_{n0}(\mathbf{r},z_i)=\int H_{n0}(\mathbf{x})e^{2\pi i(k_0-k_n)z}dz\ . \quad (4)$$

In Eq. (4) it is implicitly assumed that the inelastic transition is localized at a particular depth z_i in the crystal, a reasonable assumption for inner-shell ionization because the core electrons are tightly bound [37,38]. Then the range of the z integration along the optical axis about the depth z_i need only extend over a finite range. The projected inelastic transition potential H_{n0} describes an inelastic transition, via a Coulomb interaction, at the depth z_i from an initial state of the specimen labelled 0 to a final state labelled n, and its modulus squared gives the probability of that transition occurring [35].

The integration in Eq. (2) is over an area in the diffraction plane defined by the EELS detector and in the case of simulating STEM EDX all energy-loss electrons may lead to the emission of an X-ray and the integration is over the whole diffraction plane. If the integration area D is sufficiently large (always the case for EDX) then the exponential term effectively becomes a delta function, $\delta(\mathbf{r}-\mathbf{r}')$, and we can make the approximation that

$$\begin{aligned}W(\mathbf{r},\mathbf{r}',z_i)&\approx W(\mathbf{r},\mathbf{r},z_i)\delta(\mathbf{r}-\mathbf{r}')\\&=\frac{2\pi m}{h^2}\sum_{n\neq 0}\frac{1}{k_n}|H_{n0}(\mathbf{r},z_i)|^2\delta(\mathbf{r}-\mathbf{r}')\\&\equiv 2V(\mathbf{r},z_i)\delta(\mathbf{r}-\mathbf{r}')\ ,\end{aligned} \quad (5)$$

where $W(\mathbf{r},\mathbf{r},z_i)$ are the diagonal terms in Eq. (2) (anticipating integration up over the delta function) and the factor of two in the last line has been inserted for consistency with the conventional definition of the local effective scattering potential $V(\mathbf{r},z_i)$.

With the approximation in Eq. (5), Eq. (1) reduces to

$$F(\mathbf{P})=\frac{4\pi}{h\nu}\sum_{j,i}\int|\psi_{0,j}(\mathbf{P},\mathbf{r},z_i)|^2V(\mathbf{r},z_i)d\mathbf{r}\ . \quad (6)$$

This generic form has been derived previously, see for example Refs. [39–41] and the case where all energy-loss electrons are detected has been discussed in Ref. [42]. The fraction of electrons involved in ionization events now depends only on the probe intensity weighted by a local potential describing the inelastic scattering. Then only the diagonal terms $\psi^*_{0,j}(\mathbf{P},\mathbf{r},z_i)\psi_{0,j}(\mathbf{P},\mathbf{r},z_i)=|\psi_{0,j}(\mathbf{P},\mathbf{r},z_i)|^2$ in Eq. (1) contribute and the measurement is no longer sensitive to the relative phase of the probe at different spatial points. Put another way: if the detector is sufficiently large then all the inelastic intensity for the class of inelastic interaction we are considering falls inside the detector and the phase of $\psi_{0,j}(\mathbf{P},\mathbf{r},z_i)$ ceases to affect the inelastic signal. The signal has become incoherent, which is the case for STEM EELS only if the detector aperture is large and is always the case for STEM EDX for, as pointed out in Section 1.

Now let us consider the simulation of an EFTEM image. If we ionize an atom α which is at a depth z_i in the specimen, then we may write the "wave function" of the incident electron after inelastic scattering as [34,35]

$$\psi_{\alpha,n,j}(\mathbf{r},z_i)=\frac{m}{2\pi ih^2k_n}H_{\alpha,n0}(\mathbf{r},z_i)\psi_{0,j}(\mathbf{r},z_i)\ , \quad (7)$$

where $\psi_{0,j}(\mathbf{r},z_i)$ is the auxilliary function for the probing electron at the depth z_i, i.e. the quantity in Eq. (1) with the parameter $\mathbf{P}$ suppressed, and $H_{\alpha,n0}(\mathbf{r},z_i)$ is the projected transition potential in Eq. (4) labelled to show it is associated with the ionization of atom α. The EFTEM image is then calculated as

$$I(\mathbf{r})=\sum_{\alpha,n,j}|\psi_{\alpha,n,j}(\mathbf{r},t)\otimes T(\mathbf{r})|^2\ , \quad (8)$$

where $\psi_{\alpha,n,j}(\mathbf{r},t)$ is the wave function in Eq. (7) transmitted to the exit surface of the specimen of thickness t and is convolved with the transfer function $T(\mathbf{r})$ of the objective lens. In other words, the imaging is built up incoherently by considering the contribution from all possible final states n for each atom α pertinent to the edge under consideration and then summing over a suitable set of nuclear configurations in the QEP model.

3. Simulation for elemental mapping using STEM EELS

We will now discuss some issues which show the essential nature of simulation in understanding and reliably interpreting elemental maps obtained using STEM EELS. Elemental maps taken using the Mn L-edge down two different zone axes, on the same specimen as in Fig. 1, are shown in Fig. 2. Down the [001] zone axis, shown in Fig. 2(a), the signal has a maximum centered on the Mn/O columns. However, in Fig. 2(b), for the [111] zone axis, the Mn signal is smallest on the Bi/Sr/Mn columns, the only columns containing Mn atoms. The greyscale images, plotting minimum to maximum as black to white, obscure the relatively low contrast variation which is more obvious in the experimental data than the simulated data. The dip at the Bi/Sr/Mn columns is a consequence of the strong thermal scattering of the probe away from the column and the stronger signal between these columns is a consequence of probe spreading towards the Mn-containing columns. The brighter ring about the Bi/Sr/Mn columns indicates the range of significant interaction with the delocalized ionization potential.

So, in Fig. 2, we have encountered our first example of where the unwary might give a wrong interpretation to an EELS elemental map and simulations have revealed the physics behind this "surprise". A more subtle manifestation of thermal diffuse scattering, leading to an apparent contrast reversal, was encountered in EELS elemental mapping of Si down the [110] zone axis using the L-shell to generate atomic-scale 2D elemental maps using electrons from different regions of the Si core-loss spectrum within the L-edge [43]. Elemental maps constructed using energy windows close to the edge (143–163 eV) and substantially above the edge (280–300 eV) showed a reversal of contrast so that, for the lower energy-loss window, maxima occurred between the atomic columns. Simulation showed that this unexpected result arose because probe spreading from an open channel ultimately allows for more interaction with the delocalized transition potentials of more

Please cite this article as: L.J. Allen, Simulation in elemental mapping using aberration-corrected electron microscopy, Ultramicroscopy (2017), http://dx.doi.org/10.1016/j.ultramic.2017.03.001

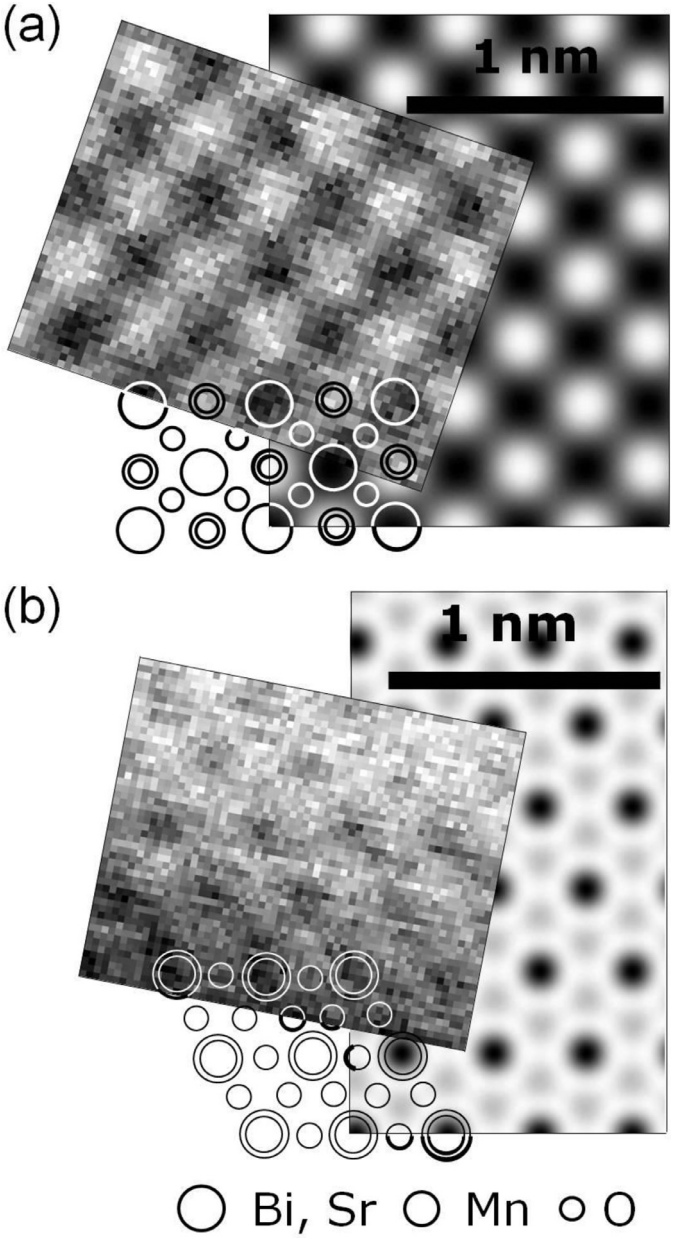

Fig. 2. Comparison between experiments (tilted images) and simulations of $Bi_{0.5}Sr_{0.5}MnO_3$ oriented down the (a) [001] zone axis and (b) [111] zone axis for the Mn $L_{2,3}$-edge EELS elemental map. The atomic structure is indicated. The elemental maps were generated by integrating the EELS spectra over a 30 eV window above the ionization threshold. The simulations assume a 330 Å sample in (a) and a 400 Å thick sample in (b). Experimental details are given in Ref. [8].

Si atoms than when the probe is placed upon a column and scattered away due to thermal scattering. For the window further from the edge the effective interaction is more localized and a contrast reversal does not occur.

However it would be wrong to assume that thermal diffuse scattering always leads to a decrease in the signal when the probe is on a column. Forbes et al. [30] reported elemental maps for O in $SrTiO_3$ down the [001] zone axis where, when the STEM probe was above the columns containing both Ti and O, more signal was obtained than for those containing only O despite the linear density of O atoms in both types of columns being the same. This is consistent with the results of a contemporary study by Dudeck et al. [44]. It is indeed thermal diffuse scatteirng that was responsible for these curious results and contribution from thermally scattered

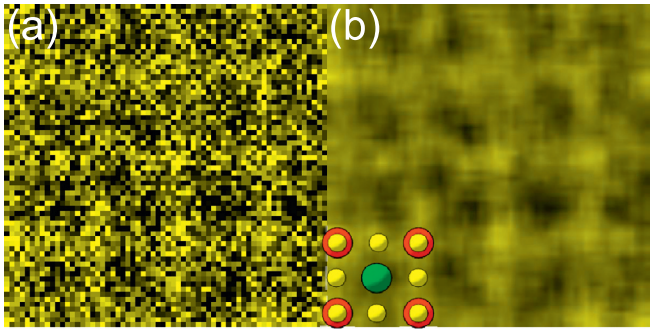

Fig. 3. (a) A STEM EDX elemental map of ⟨001⟩ $SrTiO_3$ monitoring the O K_α-line for a single scan (raw data). In (b) the result of applying a 5 × 5 pixel moving-average square window to the original data is shown. The projected structure is indicated. The positions of Ti/O columns are indicated by the red and smaller inset yellow circles, O columns by small yellow circles and the larger green circle indicates the position of an Sr column. (For interpretation of the references to colour in this figure legend, the reader is referred to the web version of this article.)

electrons was also the explanation for the same effect observed in a STEM EDX map. We will discuss this phenomenon further in the next section.

As an application of elemental mapping, simulation in tandem with 2D atomic-resolution elemental maps for a catalytic Ce-Zr mixed oxide nanocrystal have shown that in a specimen showing enhanced redox performance, obtained after redox-cycling treatments, local compositional deviations at the atomic scale are present [12]. These results were at variance with a previously proposed “ideal pyrochlore structure” for the material. We also note that the possibility of quantitative, absolute scale elemental mapping using STEM EELS has been explored in some detail [45]. And, lastly, we point out that, if the structure is reliably determined via elemental mapping then the effects of channelling and thermal diffuse scattering can be removed from EELS fine structure so that bonding effects may be examined without these complicating the picture [46,47].

4. Simulation for elemental mapping using STEM EDX

Experimental elemental maps based on EDX bear out the thesis that such maps are likely to be more directly interpretable [19]. However behaviour which may seem anomalous at first sight can occur. Consider the elemental map shown in Fig. 3 [30], obtained using an accelerating voltage of 200 kV and a probe-forming convergence semi-angle of 23 mrad. The specimen thickness was approximately 700 Å. A map for a single two-dimensional scan based on the O K-edge is shown in Fig. Fig. 4(a), whereas a filtered average using a 5× 5 pixel moving-average square window is shown in Fig. 3(b). An enhancement of the signal on the Ti/O columns relative to the pure O columns is evident. The signal from thermally scattered electrons (those which have already excited a phonon, perhaps multiple times) is key to understanding the enhancement of the signal seen in the experimental data when the probe is on the column containing the heavier Ti atoms. Using the QEP model [31], it was possible to show that this is due to ionization by the thermally scattered electrons of O atoms surrounding the column (and quite far from it in some cases), as can be seen in the simulations in Fig. 4 [30,33]. The substantial contribution when the probe is on the Ti/O column from thermally scattered electrons seen in Fig. 4(b), when added to the elastic signal in Fig. 4(a), yields more signal on the Ti/O column than on the pure O columns. Note that if one considers the elastic contribution in Fig. 4(a) then the signal on the Ti/O column is less than that on pure O columns since thermal diffuse scattering means that the probe is scattered away from

Please cite this article as: L.J. Allen, Simulation in elemental mapping using aberration-corrected electron microscopy, Ultramicroscopy (2017), http://dx.doi.org/10.1016/j.ultramic.2017.03.001

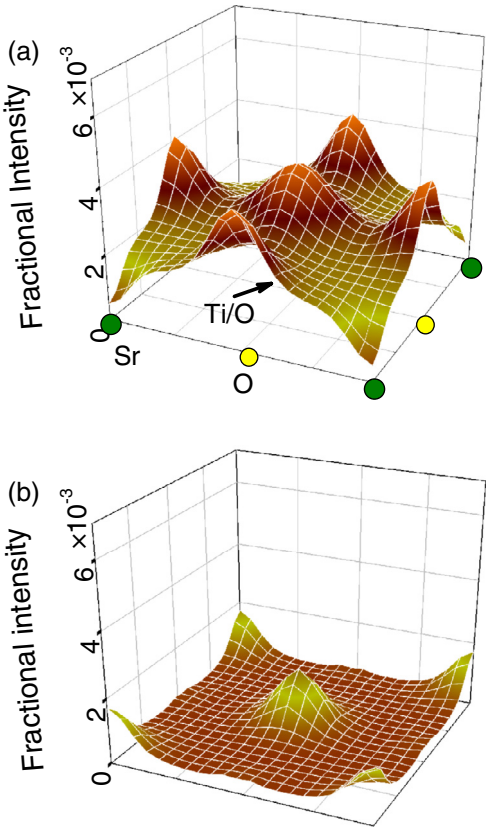

Fig. 4. Simulated contributions to an EDX elemental map using the signal in the O K-edge in ⟨001⟩ $SrTiO_3$ across a unit cell (a) due to ionization by elastically scattered electrons and (b) due to ionization by thermally scattered electrons. The projected structure is indicated: Sr columns green circles, visible O columns yellow circles and the arrow indicates the position of the Ti/O column. Parameters used: accelerating voltage 200 kV, probe-forming convergence semi-angle 23 mrad and specimen thickness 700 Å. (For interpretation of the references to colour in this figure legend, the reader is referred to the web version of this article.)

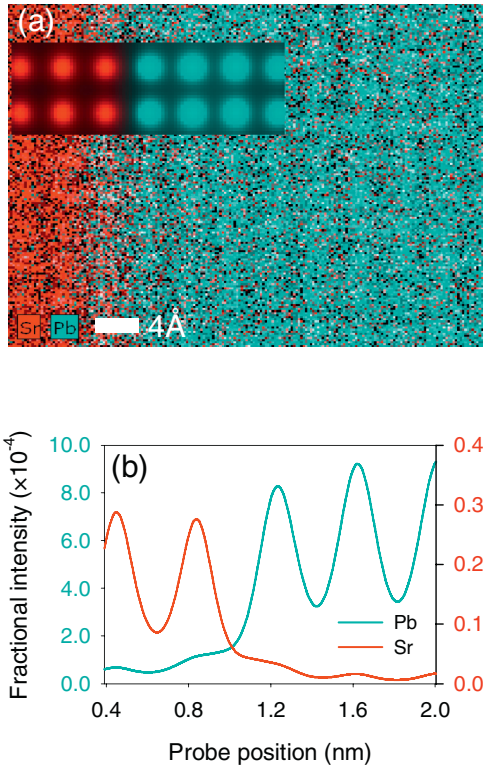

Fig. 5. (a) Atomic resolution EDX map of a $SrTiO_3$/$PbTiO_3$ interface (Sr and Pb signals are shown). Microscope imaging parameters are given in the text. Inlaid are simulated maps for Sr and Pb, assuming an atomically abrupt interface. (b) Line traces through the simulations inlaid in (a) along the columns and across the interface.

the column more in the Ti/O case than in the O case. However the electrons scattered away from the Ti/O column ionize O atoms in surrounding columns leading to an enhanced signal. Simulations are needed to gain this insight.

Fig. 5(a) shows a selected area from a composite STEM EDX map of the epitaxial (001) $SrTiO_3$-$PbTiO_3$ interface recorded along the ⟨100⟩ direction [19,48]. The Pb map was constructed from the addition of the Pb $M_{4,5}$ and $L_{2,3}$ elemental maps. The Sr elemental map was constructed from K-shell ionizations. The probe convergence semi-angle was 21.5 mrad, a probe size of approximately 1.4 Å, and with a current of 67 pA. The data presented is raw data obtained by only extracting the intensities of the characteristic absorption edges of the elements. The complete elemental map is 200 × 200 pixels and the total mapping time was approximately 300 s. The positions of the Sr and Pb atomic columns can be visualized in the map shown in Fig. 5(a). The Ti sublattice is continuous across the interface [19,48] and the Sr and Pb sublattices do not show an atomically abrupt termination at the interface, with some intermixing evident. In the first instance, this could be expected due to probe spreading and signal from thermally scattered electrons. Simulations were made with the assumption of an atomically sharp interface and are shown inlaid on Fig. 5(a). The finite size of the source was simulated by convolving the calculated map with a Gaussian with a FWHM of 1.2 Å. Line traces across the simulations are shown in Fig. 5(b). The specimen was assumed to be 500 Å thick. The simulations suggest that the interface is not atomically abrupt everywhere, since the experiment shows more mixing than is indicated by the simulation, and this cannot be accounted for by probe spreading or thermal diffuse scattering.

We next discuss what is needed to achieve quantitative elemental mapping using atomic resolution X-ray spectroscopy. The agreement between the theory described in Section 2 and experiment was carefully explored in Ref. [20] and, putting the experiment on an absolute scale by matching it to the simulations, close agreement was found. The issue of putting STEM EDX elemental maps on an absolute scale has recently been investigated [21–23]. Measured X-ray counts and EDX simulations are put on the same absolute scale using the following expression:

$$N(\mathbf{R}) = I_{\text{inc}} T F(\mathbf{R})\, \omega \left(\frac{\Omega}{4\pi}\right) D_{\text{eff}}\,. \tag{9}$$

The following factors in this equation are measurable experimentally:

- $N(\mathbf{R})$, the number of X-ray counts for a particular peak at probe position $\mathbf{R}$.
- I_{inc}, the incident beam current.
- T, the live dwell time at each probe position.
- ω, the fluorescence yield for the peak under consideration.
- $\Omega/4\pi$, the effective fraction of the whole solid angle covered by the detector.
- D_{eff}, the efficiency of the X-ray detector for the peak under consideration.

A single term remains:

- $F(\mathbf{R})$, the fraction of incident electrons resulting in ionization for a given probe position, given by Eq. (6).

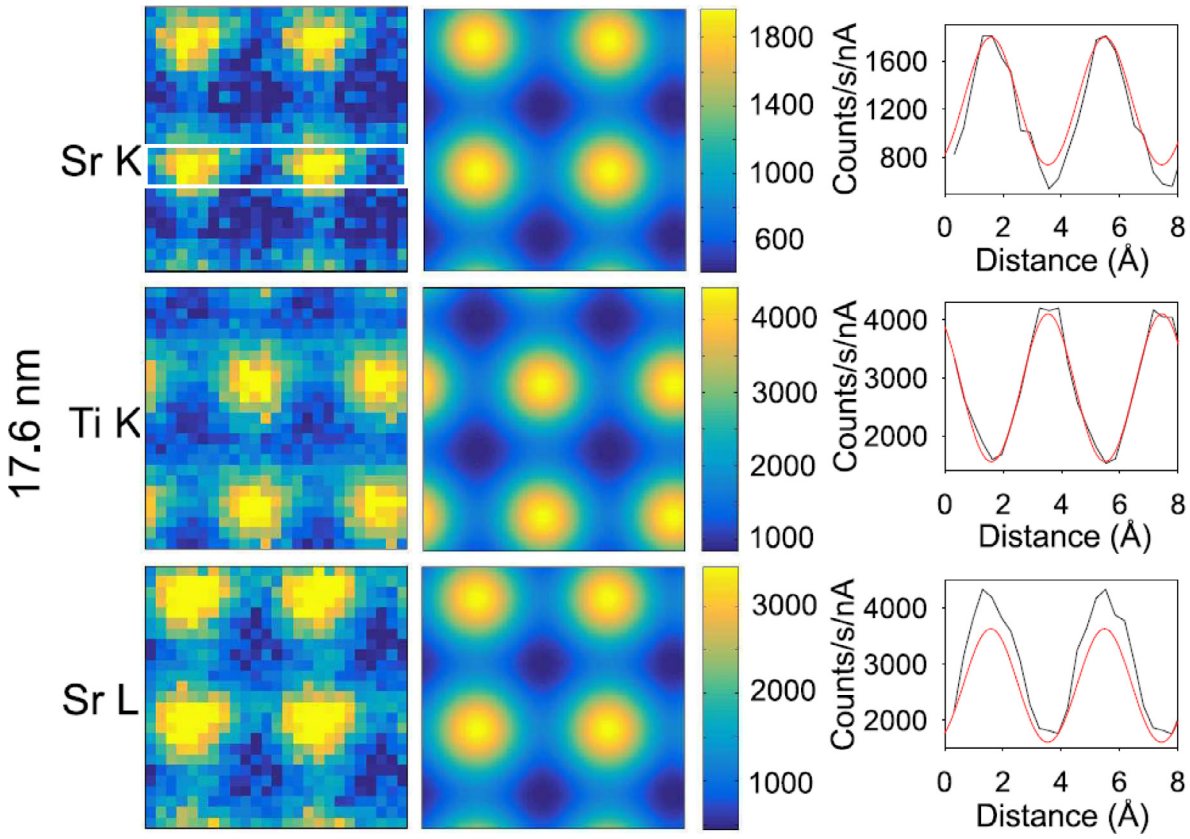

Fig. 6. Absolute-scale comparison of 2D experimental (left) and simulated (right) STEM EDX maps for a 176 Å (17.6 nm) specimen of $SrTiO_3$. The accelerating voltage is 200 keV and the probe-forming convergence angle is 19.5 mrad. Incoherence due to effective source size is modelled using a Gaussian with 1.05 Å full-width-half-maximum. Line profiles are the intensity averaged across a 1.6 Å wide strip, such as that indicated by the white rectangle for Sr K – the smoother (red line) is the simulation and the blue line is the experimental scan. (For interpretation of the references to colour in this figure legend, the reader is referred to the web version of this article.)

We can take into account absorption of X-rays in the specimen by generalizing Eq. (6) as follows:

$$F(\mathbf{R}) = \frac{4\pi}{h\nu} \sum_{j,i} \int |\psi_{0,j}(\mathbf{R}, \mathbf{r}, z_i)|^2 V(\mathbf{r}, z_i) X_{\text{abs}}(z_i) d\mathbf{r} \,, \tag{10}$$

where $X_{\text{abs}}(z_i)$ is the fraction of generated X-rays that escape the specimen from the slice at depth z_i – see Ref. [21] for more details.

The structure of the specimen is implicit in $F(\mathbf{R})$ in a nontrivial way, channeling and thermal scattering of the incident electrons playing a pivotal role in determining the $|\psi_{0,j}(\mathbf{R}, \mathbf{r}, z_i)|^2$. Therefore a structure must be assumed and $F(\mathbf{R})$ calculated and the structure refined, if necessary, until agreement is achieved between the structure and experiment. The quantity $F(\mathbf{R})$ must be determined through simulations and consistency found between theory and experiment, as shown in Fig. 6 [21]. There is no way around this if channeling and thermal diffuse scattering are significant effects, which they often are.

5. Simulation for elemental mapping using EFTEM

We can also obtain elemental maps displaying features at atomic scale using EFTEM, as done for example in Ref. [24] Chromatic aberration correction has made EFTEM more feasible [25,26]. Nevertheless, first-principles quantum mechanical calculations are needed to understand the physical information encoded in the images, in particular due to the effects of preservation of elastic contrast [25,26]. Ways of ameliorating preservation of elastic contrast have recently been proposed by Brown et al. [27].

The first achromatic elemental mapping at atomic resolution was demonstrated by Urban and co-workers [25]. Newly developed achromatic electron optics allowed the use of wide energy windows and facilitated EFTEM at the atomic scale. Elemental maps were formed using electrons that had undergone a Si $L_{2,3}$-shell energy loss, exhibiting a resolution in EFTEM of 1.35 Å. Quantum mechanical calculations from first principles were done to understand the physical information encoded in the images.

The effect that the post-ionization elastic channelling has on an EFTEM image can be seen in the simulated thickness-defocus series of EFTEM images in Fig. 7 [25]. The series was calculated for thicknesses between 50 and 400 Å and defocus values ranging between 0 and +100 Å (overfocus). It was seen that the EFTEM images appear qualitatively similar at varying specimen depths, with the intensity varying with thickness due to the channelling of the incident electron probe. The lattice contrast is most visible between defocus values of 30 to 50 Å.

A further exploration of the possibilities of atomic resolution EFTEM [26] showed qualitative agreement between experiment and simulation for EFTEM images of the Ti-$L_{2,3}$ and O K-edges for a specimen of $SrTiO_3$ oriented down the [110] zone axis. It was shown that the energy-filtered images of the Ti-$L_{2,3}$ and O K-edges are lattice images and that the background-subtracted core-loss maps were not directly interpretable elemental maps. Simulations showed that this was a result of preservation of elastic contrast, whereby the qualitative details of the image were determined primarily by elastic, coherent scattering. This effect places a constraint on the range of specimen thicknesses which yield directly interpretable elemental maps. In general, interpretation of EFTEM images is ideally accompanied by detailed simulations.

Please cite this article as: L.J. Allen, Simulation in elemental mapping using aberration-corrected electron microscopy, Ultramicroscopy (2017), http://dx.doi.org/10.1016/j.ultramic.2017.03.001

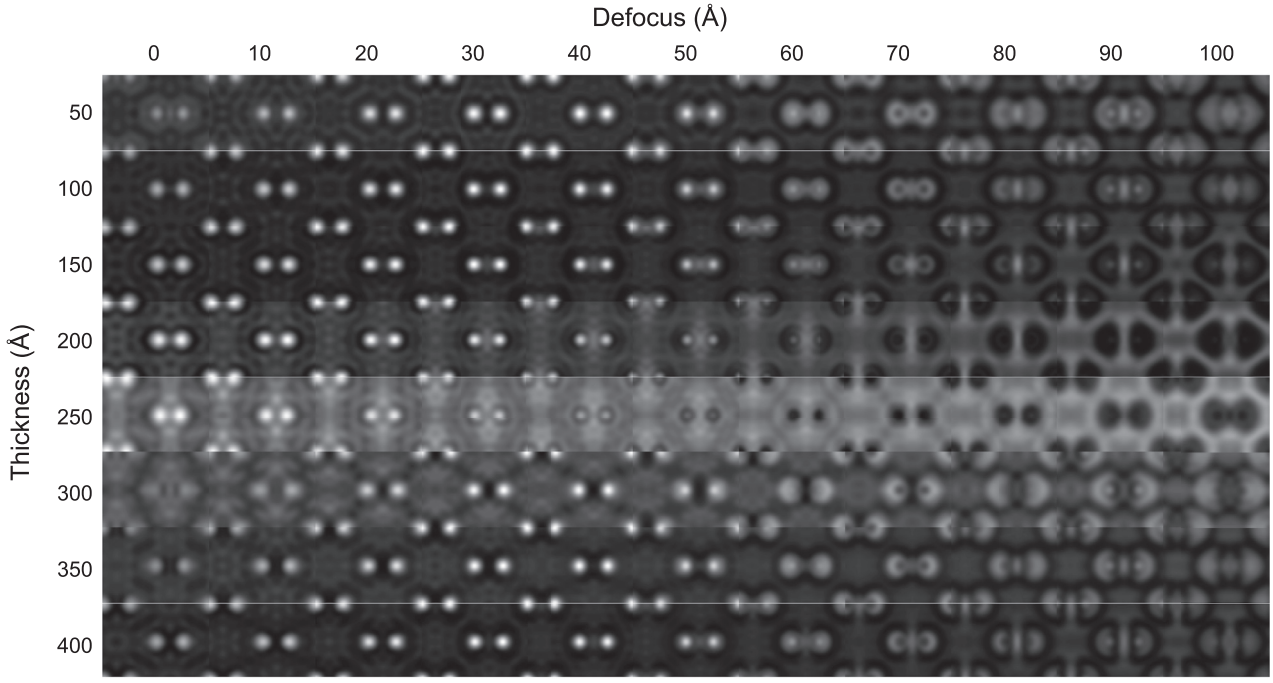

Fig. 7. Simulated thickness-defocus series of EFTEM images for the Si $L_{2,3}$-edge. An objective lens with a (negative) Cs of −8.27 μm, an objective aperture of 2 $Å^{-1}$ and varying defocus has been used. Each image has been normalized to the maximum value for a given thickness for visualization purposes.

6. Numerical modelling of elemental maps

The software package μSTEM [33,49] is capable of modelling elemental mapping using STEM EELS and EDX analysis based on inner-shell ionization.

It has been shown in Section 2 that the fractional intensity in STEM EELS can only be calculated using the local expression for the fractional intensity if most of the detector aperture is large enough that most of the inelastically scattered electrons are detected. Indeed, exact calculations using the more general "nonlocal" formulation in Section 2 have been used when exploring subtle effects which arise when the acceptance angle of an energy-loss spectrometer is comparable to the angle of the aperture used to form a scanning probe, such as the "volcanos" shown in, for example, Refs. [8,50,51]. Such calculations carry substantial computational overheads, so in μSTEM we proceed using an approximate approach, as described in the remainder of this paragraph. We initially assume that the EELS detector covers the whole solid angle, because this makes it possible to compactly parametrize scattering factors for a wide range of pertinent inner-shell ionization edges as a function of the magnitude of the momentum transfer and energy loss, so that the local potential in Eq. (6) can be rapidly calculated. Zhu et al [52]. recently proposed correcting *experimental* images for this sort of discrepancy by dividing the experimental maps by a normalized "incoherent bright field" image, the image formed with the same detector collection angle as the EELS image but integrated over the full energy range, elastic and thermal scattering included. We, instead, multiply the simulated EELS map, assuming a detector covering the whole solid angle, by a simulated incoherent bright field image assuming a detector with collection angle equal to that in the experiment (and expressed as a fraction of the incident intensity). In the quantum excitation of phonons model both elastic and thermally scattered electrons are included in the correction (other inelastic processes are a small contribution). In the absorptive model only elastically scattered electrons are included. The corrected map is automatically generated by the code.

EDX maps are calculated by integrating the EELS cross section over all possible energies above the ionization threshold and no correction is necessary for scattering outside a detector aperture, as in the case of EELS, since all ionization kinematics can lead to the production of an X-ray. The X-ray signal is assumed to be proportional to the energy-loss signal calculated in this way since the emission of X-rays, resulting from the filling of holes subsequent to ionization events, occurs isotropically for all possible energy losses and kinematics.

The μSTEM package is capable not only of simulating elemental maps for perfect crystals but also for more interesting cases such as grain boundaries [53]. It is also possible to check for the effects of surface reconstructions or amorphous surface layers. For the bulk specimens, such as those considered here, these are generally small effects but will become more important in the quest for better quantification.

7. Summary and conclusions

We have reviewed progress in the simulation of elemental mapping at the atomic scale based on the inelastic scattering of electrons due to ionization. The crucial importance of theory and simulation in interpreting and quantifying results has been highlighted. The software package μSTEM, capable of simulating STEM EELS and STEM EDX images has been discussed.

Acknowledgements

This research was supported under the Australian Research Councils Discovery Projects funding scheme (Project DP110102228). The author acknowledges the important contribution of collaborators and colleagues in the electron microscopy community to this work. In particular, the substantial contributions of the following colleagues in Melbourne to the work described here is acknowledged: Adrian D'Alfonso, Zhen Chen, Eireann Cosgriff, Christian Dwyer, Scott Findlay, Ben Forbes, Torgny Josefsson, Nathan Lugg,

Andrew Martin, Melissa Neish, Mark Oxley, Chris Rossouw, Gary Ruben, Matt Weyland and Chris Witte.

References

[1] J. Taftø, O.L. Krivanek, Site-specific valence determination by electron energy-loss spectroscopy, Phys. Rev. Lett. 48 (1982) 560.
[2] O.L. Krivanek, A.J. Gubbens, N. Dellby, Developments in EELS instrumentation for spectroscopy and imaging, Microsc. Microanal. Microstruct. 2 (1991) 315–332.
[3] O.L. Krivanek, A.J. Gubbens, N. Dellby, C.E. Meyer, Design and first applications of a post-column imaging filter, Microsc. Microanal. Microstruct. 3 (1992) 187–199.
[4] O.L. Krivanek, M.K. Kundmann, K. Kimoto, Spatial resolution in EFTEM elemental maps, J. Microsc. 180 (1995) 277–287.
[5] M. Varela, S.D. Findlay, A.R. Lupini, H.M. Christen, A.Y. Borisevich, N. Dellby, O.L. Krivanek, P.D. Nellist, M.P. Oxley, L.J. Allen, S.J. Pennycook, Spectroscopic imaging of single atoms within a bulk solid, Phys. Rev. Lett. 92 (2004) 095502.
[6] O.L. Krivanek, N. Dellby, M.F. Murfitt, M.F. Chisholm, T.J. Pennycook, K. Suenaga, V. Nicolosi, Gentle STEM: ADF imaging and EELS at low primary energies, Ultramicroscopy 110 (2010) 935–945.
[7] O.L. Krivanek, M.F. Chisholm, V. Nicolosi, T.J. Pennycook, G.J. Corbin, N. Dellby, M.F. Murfitt, C.S. Own, Z.S. Szilagyi, M.P. Oxley, S.T. Pantelides, S.J. Pennycook, Atom-by-atom structural and chemical analysis by annular dark-field electron microscopy, Nature 464 (2010) 571–574.
[8] M. Bosman, V.J. Keast, J.L.G.-M. noz, A.J. D'Alfonso, S.D. Findlay, L.J. Allen, Two-dimensional mapping of chemical information at atomic resolution, Phys. Rev. Lett. 99 (2007) 086102.
[9] K. Kimoto, T. Asaka, T. Nagai, M. Saito, Y. Matsui, K. Ishizuka, Element-selective imaging of atomic columns in a crystal using STEM and EELS, Nature 450 (2007) 702–704.
[10] D.A. Muller, L.F. Kourkoutis, M. Murfitt, J.H. Song, H.Y. Hwang, J. Silcox, N. Dellby, O.L. Krivanek, Atomic-scale chemical imaging of composition and bonding by aberration-corrected microscopy, Science 319 (2008) 1073–1076.
[11] L.J. Allen, New directions for chemical maps, Nat. Nanotechnol. 3 (2008) 255–256.
[12] S. Trasobares, M. López-Haro, M. Kociak, K. March, F. de La Peña, J.A. Perez-Omil, J.J. Calvino, N.R. Lugg, A.J. D'Alfonso, L.J. Allen, C. Colliex, Chemical imaging at atomic resolution as a technique to refine the local structure of nanocrystals, Angew. Chem. Int. Ed. 50 (2011) 868–872.
[13] C. Dwyer, Atomic-resolution core-level spectroscopy in the scanning transmission electron microscope, Adv. Imaging Electron Phys. 175 (2013) 145–199.
[14] R. Ishikawa, A.R. Lupini, S.D. Findlay, T. Taniguchi, S.J. Pennycook, Three-dimensional location of a single dopant with atomic precision by aberration–corrected scanning transmission electron microscopy, Nano Lett. 14 (2014) 1903–1908.
[15] R.F. Egerton, Electron Energy-Loss Spectroscopy in the Electron Microscope, Springer, New York, 2011.
[16] S.J. Pennycook, P.D. Nellist (Eds.), Scanning Transmission Electron Microscopy: Imaging and Analysis, Springer, New York, 2011.
[17] A.J. D'Alfonso, B. Freitag, D. Klenov, L.J. Allen, Atomic resolution chemical mapping using energy dispersive x-ray spectroscopy, Phys. Rev. B 81 (2010) 100101R.
[18] M.-W. Chu, S.C. Liou, C.-P. Chang, F.-S. Choa, C.H. Chen, Emergent chemical mapping at atomic-column resolution by energy-dispersive x-ray spectroscopy in an aberration-corrected electron microscope, Phys. Rev. Lett. 104 (2010) 196101.
[19] L.J. Allen, A.J. D'Alfonso, B. Freitag, D.O. Klenov, Chemical mapping at atomic resolution using energy-dispersive x-ray spectroscopy, MRS Bull. 37 (2012) 47–52.
[20] G. Kothleitner, M.J. Neish, N.R. Lugg, S.D. Findlay, W. Grogger, F. Hofer, L.J. Allen, Quantitative elemental mapping at atomic resolution using x-ray spectroscopy, Phys. Rev. Lett. 112 (2014) 085501.
[21] Z. Chen, A.J. D'Alfonso, M. Weyland, D.J. Taplin, L.J. Allen, S.D. Findlay, Energy dispersive X-ray analysis on an absolute scale in scanning transmission electron microscopy, Ultramicroscopy 157 (2015) 21–26.
[22] J.H. Dycus, W. Xu, A.J. D'Alfonso, X. Sang, L.J. Allen, S.D. Findlay, J.M. LeBeau, Influence of experimental conditions on quantitative atomic resolution energy dispersive X-ray spectroscopy, Ultramicroscopy 171 (2016) 1–7.
[23] Z. Chen, M. Weyland, X. Sang, W. Xu, J.H. Dycus, J.M. LeBeau, A.J. D'Alfonso, L.J. Allen, S.D. Findlay, Quantitative atomic resolution elemental mapping via absolute-scale energy dispersive X-ray spectroscopy, Ultramicroscopy 168 (2016) 7–16.
[24] N.R. Lugg, B. Freitag, S.D. Findlay, L.J. Allen, Energy-filtered transmission electron microscopy based on inner-shell ionization, Ultramicroscopy 110 (2010) 981–990.
[25] K.W. Urban, J. Mayer, J.R. Jinschek, M.J. Neish, N.R. Lugg, L.J. Allen, Achromatic elemental mapping beyond the nanoscale in the transmission electron microscope, Phys. Rev. Lett. 110 (2013) 185507.
[26] B.D. Forbes, L. Houben, J. Mayer, R.E. Dunin-Borkowski, L.J. Allen, Elemental mapping in achromatic atomic-resolution energy-filtered transmission electron microscopy, Ultramicroscopy 147 (2014) 98–105.
[27] H.G. Brown, A.J. D'Alfonso, B.D. Forbes, L.J. Allen, Addressing preservation of elastic contrast in energy-filtered transmission electron microscopy, Ultramicroscopy 160 (2016) 90–97.
[28] M.P. Oxley, E.C. Cosgriff, L.J. Allen, Nonlocality in imaging, Phys. Rev. Lett. 94 (2005) 203906.
[29] L.J. Allen, S.D. Findlay, M.P. Oxley, M. Bosman, V.J. Keast, E.C. Cosgriff, G. Behan, P.D. Nellist, A.I. Kirkland, Theoretical Interpretation of Electron Energy-loss Spectroscopic Images, in: Electron Microscopy and Multiscale Modeling - EMMM-2007: An International Conference, Vol. 999, AIP Publishing, 2008, pp. 32–46.
[30] B.D. Forbes, A.J. D'Alfonso, R.E.A. Williams, R. Srinivasan, H.L. Fraser, D.W. McComb, B. Freitag, D.O. Klenov, L.J. Allen, Contribution of thermally scattered electrons to atomic resolution elemental maps, Phys. Rev. B 86 (2012) 024108.
[31] B.D. Forbes, A.V. Martin, S.D. Findlay, A.J. D'Alfonso, L.J. Allen, Quantum mechanical model for phonon excitation in electron diffraction and imaging using a Born-Oppenheimer approximation, Phys. Rev. B 82 (2010) 104103.
[32] N.R. Lugg, B.D. Forbes, S.D. Findlay, L.J. Allen, Atomic resolution imaging using electron energy-loss phonon spectroscopy, Phy. Rev. B 91 (14) (2015) 144108.
[33] L.J. Allen, A.J. D'Alfonso, S.D. Findlay, Modelling the inelastic scattering of fast electrons, Ultramicroscopy 151 (2015) 11–22.
[34] W. Coene, D.V. Dyck, Inelastic scattering of high-energy electrons in real space, Ultramicroscopy 33 (1990) 261–267.
[35] C. Dwyer, Multislice theory of fast electron scattering incorporating atomic inner-shell ionization, Ultramicroscopy 104 (2005) 141–151.
[36] S.D. Findlay, M.P. Oxley, L.J. Allen, Modeling atomic-resolution scanning transmission electron microscopy images, Microsc. Microanal. 14 (2006) 48–59.
[37] D.K. Saldin, P. Rez, The theory of the excitation of atomic inner-shells in crystals by fast electrons, Philos. Mag. B 55 (1987) 481–489.
[38] V.W. Maslen, On the role of inner-shell ionization in the scattering of fast electrons by crystals, Philos. Mag. B 55 (1987) 491–496.
[39] D. Cherns, A. Howie, M.H. Jacobs, Characteristic x-ray production in thin crystals, Zeitschrift für Naturforschung A 28 (1973) 565–571.
[40] K. Ishizuka, Prospects of atomic resolution imaging with an aberration-corrected STEM, J. Electron Microsc. 50 (2001) 291–305.
[41] L.J. Allen, S.D. Findlay, M.P. Oxley, C.J. Rossouw, Lattice-resolution contrast from a focused coherent electron probe, Part I, Ultramicroscopy 96 (2003) 47–63.
[42] R.H. Ritchie, A. Howie, Inelastic scattering probabilities in scanning transmission electron microscopy, Philos. Mag. A 58 (5) (1988) 753–767.
[43] P. Wang, A.J. D'Alfonso, S.D. Findlay, L.J. Allen, A.L. Bleloch, Contrast reversal in atomic-resolution chemical mapping, Phys. Rev. Lett. 101 (2008) 236102.
[44] K.J. Dudeck, M. Couillard, S. Lazar, C. Dwyer, G.A. Botton, Quantitative statistical analysis, optimization and noise reduction of atomic resolved electron energy loss spectrum images, Micron 43 (2012) 57–67.
[45] H.L. Xin, C. Dwyer, D.A. Muller, Is there a stobbs factor in atomic-resolution STEM-EELS mapping? Ultramicroscopy 139 (2014) 38–46.
[46] N.R. Lugg, M. Haruta, M.J. Neish, S.D. Findlay, T. Mizoguchi, K. Kimoto, L.J. Allen, Removing the effects of elastic and thermal scattering from electron energy-loss spectroscopic data, Appl. Phys. Lett. 101 (2012) 183112.
[47] N.R. Lugg, M.J. Neish, S.D. Findlay, L.J. Allen, Practical aspects of removing the effects of elastic and thermal diffuse scattering from spectroscopic data for single crystals, Microsc. Microanal. 20 (2014) 1078–1089.
[48] D. Klenov, B. Freitag, H.S. von Harrach, A.J. D'Alfonso, L.J. Allen, Chemical mapping at the atomic level using energy dispersive x-ray spectroscopy, Microsc. Microanal. 17 (S2) (2011) 598–599.
[49] μSTEM, http://tcmp.ph.unimelb.edu.au/mustem/muSTEM.html.
[50] M.P. Oxley, M. Varela, T.J. Pennycook, K. van Benthem, S.D. Findlay, A.J. D'Alfonso, L.J. Allen, S.J. Pennycook, Interpreting atomic-resolution spectroscopic images, Phys. Rev. B 76 (2007) 064303.
[51] A.J. D'Alfonso, S.D. Findlay, M.P. Oxley, L.J. Allen, Volcano structure in atomic resolution core-loss images, Ultramicroscopy 108 (2008) 677–687.
[52] Y. Zhu, A. Soukiassian, D.G. Schlom, D.A. Muller, C. Dwyer, Towards artifact-free atomic-resolution elemental mapping with electron energy-loss spectroscopy, Appl. Phys. Lett. 103 (2013) 141908.
[53] M.M. McGibbon, N.D. Browning, M.F. Chisholm, A.J. McGibbon, S.J. Pennycook, V. Ravikumar, V.P. Dravid, Direct determination of grain boundary atomic structure in $SrTiO_3$, Science 266 (1994) 102–104.

Please cite this article as: L.J. Allen, Simulation in elemental mapping using aberration-corrected electron microscopy, Ultramicroscopy (2017), http://dx.doi.org/10.1016/j.ultramic.2017.03.001